World Academy of Science, Engineering and Technology
International Journal of Humanities and Social Sciences
Vol:15, No:10, 2021

Machine Learning Methods for Flood Hazard Mapping

S. Zappacosta, C. Bove, M. Carmela Marinelli, P. di Lauro, K. Spasenovic, L. Ostano, G. Aiello, M. Pietrosanto

***Abstract*—**This paper proposes a neural network approach for assessing flood hazard mapping. The core of the model is a machine learning component fed by frequency ratios, namely statistical correlations between flood event occurrences and a selected number of topographic properties. The classification capability was compared with the flood hazard mapping River Basin Plans (Piani Assetto Idrogeologico, acronimed as PAI) designed by the Italian Institute for Environmental Research and Defence, ISPRA (Istituto Superiore per la Protezione e la Ricerca Ambientale), encoding four different increasing flood hazard levels. The study area of Piemonte, an Italian region, has been considered without loss of generality. The frequency ratios may be used as a standalone block to model the flood hazard mapping. Nevertheless, the mixture with a neural network improves the classification power of several percentage points, and may be proposed as a basic tool to model the flood hazard map in a wider scope.

***Keywords*—**Flood modeling, hazard map, neural networks, hydrogeological risk, flood risk assessment.

I. Introduction

A flood event refers to a situation where the river flow and water level rise unexpectedly [1], [2]. Forecasting or modeling climatic-hydrologic factors triggering such phenomena is a complex task, nevertheless the dependence of flood intensity from the geographical location and the climatic and geological conditions can be investigated [3], [4].

Floods are one of the most dangerous natural disasters, either in terms of material damages and in terms of human losses [5], [6]. Therefore, assessing the flood hazard is a key task for any risk management program [7], [8].

Risk analysis is the study of the underlying uncertainty of the consequences of a specific hazard in terms of statistical expected damages [9]. Indeed, risk is evaluated through the correlation between the frequency of a natural disastrous event and the intensity of the corresponding damages. Present paper focuses on floods, inspecting the expected degree of loss after such events. As far as the flood is concerned, the $Risk$ at a given position pos may be modelled by:

$$Risk(pos) = F(Hazard(pos), Vulnerability(pos), Elements(pos))$$

where F is a generic function, monotonically non-decreasing on every component.

This paper focuses on the hazard component, $Hazard(pos)$, encoding flood occurrence probability. The goal is to design an artificial intelligence-based solution to estimate that probability is depending on some morphological features observed in a specific geographic position pos. It turns out that such an estimate is time-invariant in the short run, since morphological features are supposed to vary with very low time-frequency.

ISPRA has deployed a flood hazard risk map called PAI. The PAI map encodes three different levels, according to an increasing time-frequency, namely 1, 2, and 3. The value of hazard in any position is assessed on the basis of historical recorded events.

To estimate the flood probability map, a combination of data-driven techniques with remote sensing and geographical information systems was mixed with a machine learning module. Namely, the frequency ratio approach [10], on twelve topographic properties was combined with a multilayer perceptron [10]-[12]. Each class of conditioning factor was weighted using the frequency ratio approach and entered as input for feed-forward neural network to optimize all the parameters.

Piemonte, an Italian region with a wide range of topographic features, has been selected as a study area, and used to show model performances.

II. Materials

The Italian region Piemonte was considered as a study area, with a spatial resolution of 10x10 meters. Every layer involved with the model may be represented as a matrix with shape:

- width: 20.367 pixels
- height: 26.642 pixels

Because of the boundaries (see Fig. 1) only a portion of the 542.617.614 pixels is admissible. Namely, we have the following size

- inner: 253.648.261 pixels
- outer: 288.969.353 pixels

The following twelve conditioning factors are used to assess flood hazard.

Static Data

PAI - Hydraulic Hazard Scenarios

The Extract Plan for Hydrogeological Asset (PAI), designed by ISPRA provides the hydrogeological hazards (see Fig. 2 for a detailed view of the Piemonte region). It is divided into the part of landslides and the part of floods. The flood plan represents the hazard maps and describes scenarios with different probability of occurrence:

Marco Pietrosanto is with Omnitech Research Group, Italy (e-mail: marco.pietrosanto@omninext.it).

- P3: the highest probability of occurrence, has smaller extensions than the others, but shorter return period, from 20 to 50 years
- P2: the average probability of occurrence, has greater extensions than P3 but has a higher return period from 100 to 200 years
- P1: the lowest probability of occurrence, has a maximum extension and is associated with extreme and catastrophic events with a return period between 300 and 500 years.

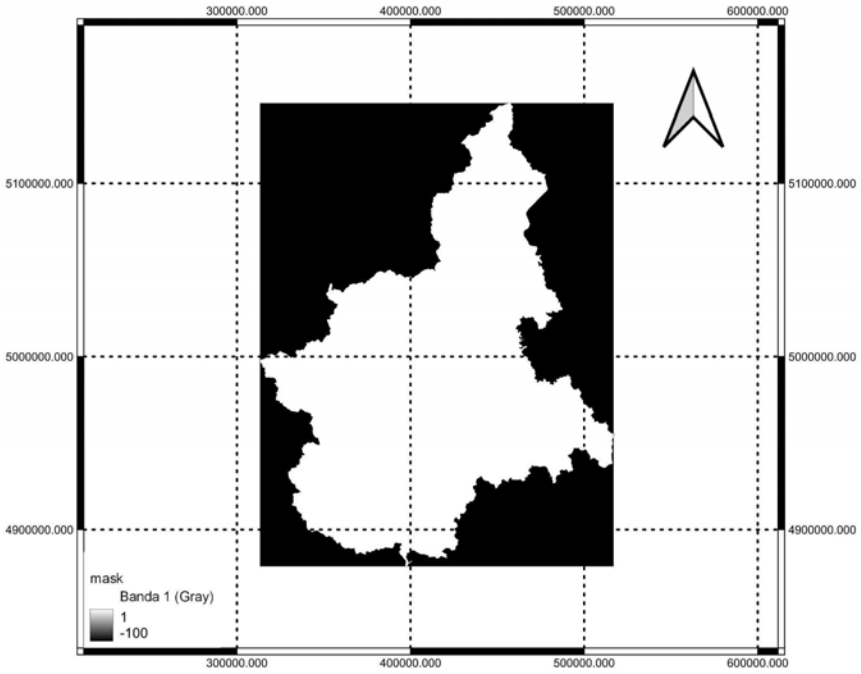

Fig. 1 Mask raster of the study are of Piemonte (admissible pixels are white)

Areas P3 and P2 fall within P1 areas, since they encode monotonic probabilities. Therefore, the levels do not add up, they represent the highest hazard level. This layer will be used to build the target of every model, in such a way to have supervised training.

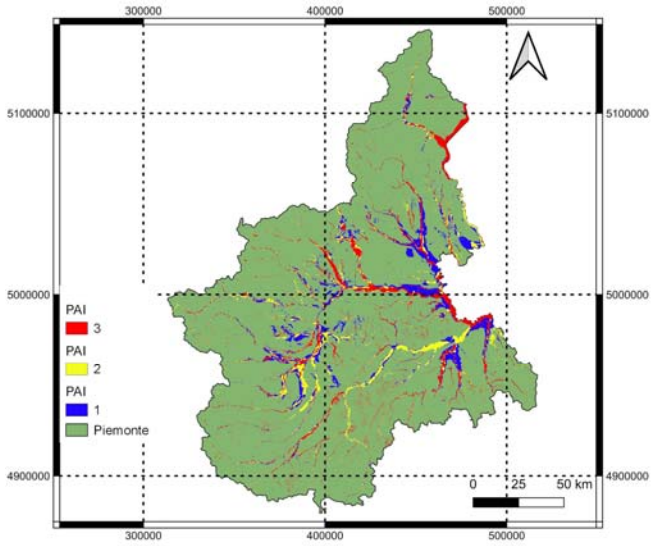

Fig. 2 Hydro-geological hazards raster of the study are of Piemonte

Digital Terrain Model and Derived Parameters

The main data are the DTM (Digital Terrain Model), it represents the topography of the study area with a pixel resolution of 10x10 meters. Most of the static data (such as: Elevation, Slope, Aspect, Curvature, STI, TWI, TRI, STI and Distance from rivers) derive from it.

All topographic parameters are extracted from the DTM, this leads to the fact that the accuracy of the DTM affects the result of the other parameters.

Elevation

The main factor for studying a flood is the altitude, in fact a flood is highly unlikely to occur in areas at high altitudes. Streams will always move from higher elevations to lower elevations and will always gather in flat areas. In fact, the topography is directly connected to the flows. See Fig. 6 for the corresponding raster of the study area of Piemonte.

Aspect

The aspect is the direction of the slope. An aspect of 0 means that the slope faces North, 90 faces East, 180 South and 270 West.

Flat areas will return nan values. In fact, an area with a slope equal to 0 will not have an exposure direction. See Fig. 8 for the corresponding raster of the study area of Piemonte.

Slope

Another factor that influences the flow path is the slope, in fact the water will always move on the higher slope topography, channeling into the *impluvium*.

As the slope increases, the water infiltration time decreases and therefore a greater quantity of water enters the network of *impluvia* and channels causing an accumulation of water and therefore a probable flood [13]. The slope is also responsible for the speed of the runoff. Higher slopes will have higher flow rates and also greater erosion and transport force, in relation to the substrate. This can affect the flux density. The hydraulic action dissolves the materials along the sliding surface changing the flow solution. Furthermore, the same hydraulic action impacts the sides and bed of the channel, displacing the materials and making them available for transport as part of the flow load. Lighter materials are transported in suspension, while heavier materials are transported by traction and jumping on the bed, eroding the channel by abrasion [14]. See Fig. 7 for the corresponding raster of the study area of Piemonte.

Curvature

In relation to the slope there is the exposure of the slope. It is divided into 3 classes, concave, convex and flat. These classes in turn are divided into 9 categories which reflect the shape of the slope profile (see Fig. 4). These shapes influence the path of water flows during the events that trigger the floods.

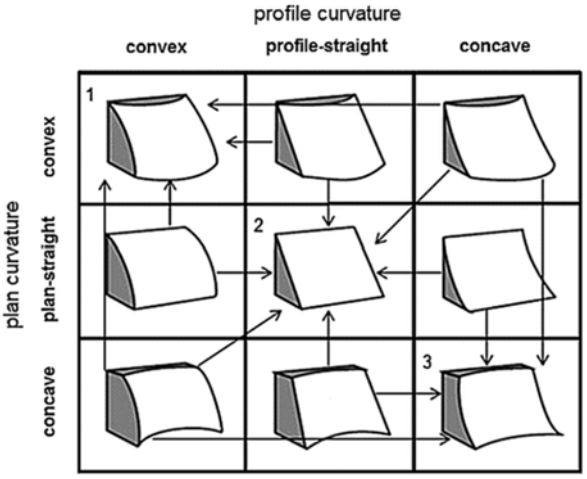

Fig. 3 The nine categories of slope shapes with respect to convexity and concavity [15]

In order to quantify the parameters that affect the power of the flows in relation to the slope two indices were calculated (namely, Stream Power Index (SPI) and Topographic Wetness Index (TWI)) according to the formulas described below [16]. See Fig. 9 for the corresponding raster of the study area of Piemonte.

Stream Power Index

The SPI is defined by: SPI = ln(*CA* · tan α) where *CA* is the catchment area[1] and α is the slope angle. This index characterizes the areas subject to erosion. SPI can be used to describe potential flow erosion at the given point of the topographic surface. As catchment area and slope gradient increase, the amount of water contributed by upslope areas and the velocity of water flow increase, hence SPI and erosion risk increase. See Fig. 12 for the corresponding raster of the study area of Piemonte.

Topographic Wetness Index

The TWI is defined by: TWI = ln(*B* / tan α) where *B* is the upstream contributing area per unit width orthogonal to the flow direction and α is the slope angle. This index is a useful estimate of where the water will accumulate in an area with elevation differences. In the case of a flat area, accumulation numbers will be very large, so TWI will not be a relevant variable. See Fig. 15 for the corresponding raster of the study area of Piemonte.

Sediment Transport Index

The Sediment Transport Index (STI) is defined by: STI = (m + 1) · (CA / 22.13) ^{m} · sin (α / 0.0896) ^{n} where *CA* is the specific catchment area, α is the slope, m is the contributing area exponent (usually set to 0.4) and n is the slope exponent (usually set to 1.4). It can be used to describe the erosive and depositional processes [16]. See Fig. 13 for the corresponding raster of the study area of Piemonte.

Topographic Ruggedness Index

The Topographic Ruggedness Index (TRI) is defined by: TRI = $\sqrt{\sum_{ij=-1}^{1}\left(X_{ij}-X_{00}\right)^2}$ where X_{ij} are the values of the 8 cells surrounding the central cell X_{00} as shown by Fig. 4 [17]. It was calculated automatically via the GDAL library in OSGeo4W. It is used to quantify the heterogeneity of the territory and obtained by calculating the difference in elevation between the adjacent cells of the DTM. See Fig. 4 for the corresponding raster of the study area of Piemonte.

-1,-1	0,-1	1,-1
-1,0	0,0	1,0
-1,1	0,1	1,1

Fig. 4 Indices of the 9 cells

Distance from River

The last parameter derived from the DTM is the distance from rivers. It was developed in 2 stages:

1. the extraction of rivers and waterways from the DTM, using the *r.stream.extract* algorithm of the Grass78 library with QGis software.
2. the creation of the distances, in meters, from the lines extracted using the Euclidean distance in QGis.

This parameter is fundamental as floods often occur near rivers or bodies of water. Therefore, the proximity to it represents a higher danger. See Fig. 6 for the corresponding raster of the study area of Piemonte.

The lithological map and the type of soil are important parameters for identifying areas subject to flooding. In fact, the

[1] The catchment area (CA) is an area of a closed figure formed by a contour segment at a given point of the topographic surface and two flow lines coming from upslope to the contour segment ends. The unit of measurement is m^2.

type of soil affects its drainage processes based on the degree of permeability and texture.

Soil

The soil type was elaborated by taking into account the percentages of sand, silt and clay and plotting the data in the ternary diagram (see Fig. 5).

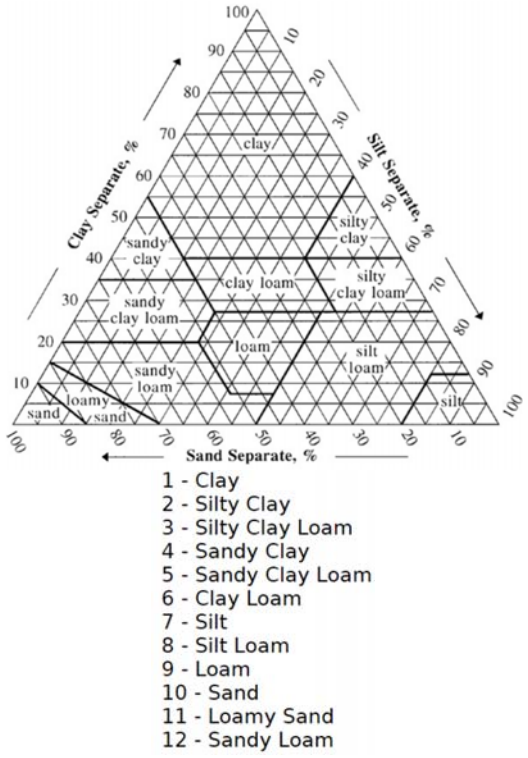

Fig. 5 Ternary diagram for the classification of soils [19]

The information was taken from [20] and processed in QGis via Soil Texture Classification from the SAGA library. See Fig. 17 for the corresponding raster of the study area of Piemonte.

Lithology

We considered the following lithologies:

1. Alluvial deposits in the plain and valley areas (Rissian age-current)
2. Morainic deposits (Quaternary)
3. Banks and clayey levels (Villafranchiano)
4. Fine to medium sands (Asti sands)
5. Clays and clayey marls (Upper Miocene-Middle Pliocene)
6. Layers of marl (Middle Miocene)
7. Marly siltstones (Upper Oligocene-Miocene)
8. Sandstones (Arenaria di Ranzano, Oligocene)
9. Alternations of clays (Cretaceous-Eocene)
10. Serpentinites (Piemonte area, Jurassic-Cretaceous)
11. Calcescisti (Piemonte area, Jurassic-Cretaceous)
12. Dolomite and limestone (Mesozoic Units)
13. Gneiss minutes (Massifs of Dora-Maira, Sesia-Lanzo)
14. Gneiss occhiadini (Massifs Monte Rosa and Val d`Ossola)
15. Granites (Migmatites, ercinic and late-alpine)
16. Other

These lithologies can be grouped into 4 types (see Fig. 16 for the corresponding raster of the study area of Piemonte):

1. clastic rocks
2. intrusive rocks
3. metamorphic rocks
4. sedimentary rocks

In clastic rocks are included:

- Clay banks and levels: alternations of clays in banks and in lists with sandy and gravelly levels of fluvial-lacustrine origin (Villafranchian age)
- Alternations of clay: alternations of clays with calcarenites (arenaceous limestones), elements of dolomitic limestones from Trias, encrinites from Lias, marly limestones and locally granite pebbles (Cretaceous-Eocene age).
- Morainic deposits: accumulation of rock fragments, even in the order of one meter, sand and clay of erosive origin by the movement of the ice that it deposits after its melting (Quaternary age).
- Ranzano sandstones: arenaceous-conglomeratic formation formed by several sedimentary bodies of turbidite origin (Oligocene age)
- Clays and clayey marls: alternation of clays and clayey marls (from 65 to 75% of clayey part and the rest limestone, middle-lower Miocene age)
- Fine to medium sands: alternation of fine (125μ to 250μ) and medium (250 medie to 500μ) sands. Incoherent or locally cemented yellow sands generally homogeneous with the presence of ripple (upper Plieocene age)
- Alluvial deposits: eluvius-colluvial deposits (gravels, sands and poorly classified clays) with relict rocks, due to the erosive action and transport of water (Rissian age)
- Marly siltstones - Termô Fôrà complex: siltstones, sands and conglomerates. Alternations of silts and marly-siliceous limestones (Miocene age)

In intrusive rocks are included:

- Granites: coarse-grained acidic plutonic rocks made up of quartz (20-60%), alkaline feldspar, plagioclase and mafic minerals. It is formed by fractional crystallization within the earth's crust between 10 and 30 km deep (Paleozoic age)

In metamorphic rocks are included:

- Serpentinites: metamorphic rocks made up almost exclusively of minerals from the serpentine group such as antigorite, lizardite and chrysotile, deriving from hydration processes of mafic and ultramafic rocks. Serpentinization is a low-temperature metamorphic process that tends to transform anhydrous minerals (pyroxene and olivine) into hydrated minerals. Depending on the type of rock, particular minerals such as brucite and magnetite can be formed (Triassic-Jurassic age)
- Gneiss minutes: rocks formed at great depth, due to the changed conditions of pressure and temperature, in the areas of convergence of two plates. Estimated metamorphic conditions of 1.4-1.6 Gpa and 500-600 °C (Carboniferous-Permian age)
- Gneiss Occhiadini: medium-large-grained rocks, with a

generally granitic composition, characterized by large oval-shaped feldspar crystals (porphyroclasts) called "augen". These are rocks with a medium-high metamorphic degree (Triassic - Jurassic age)

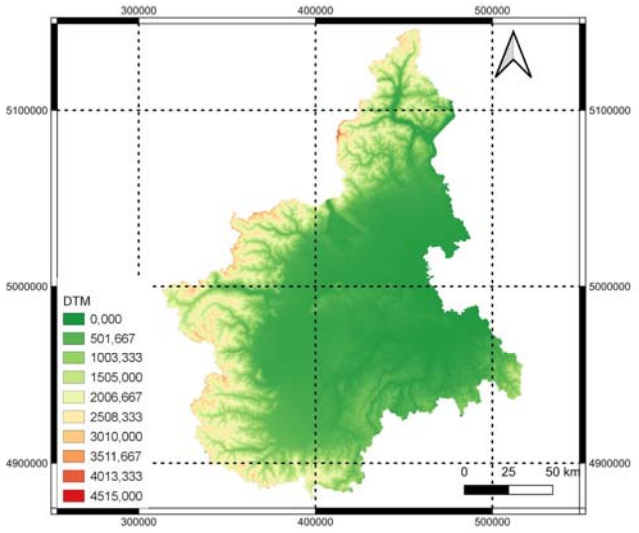

Fig. 6 Elevation raster

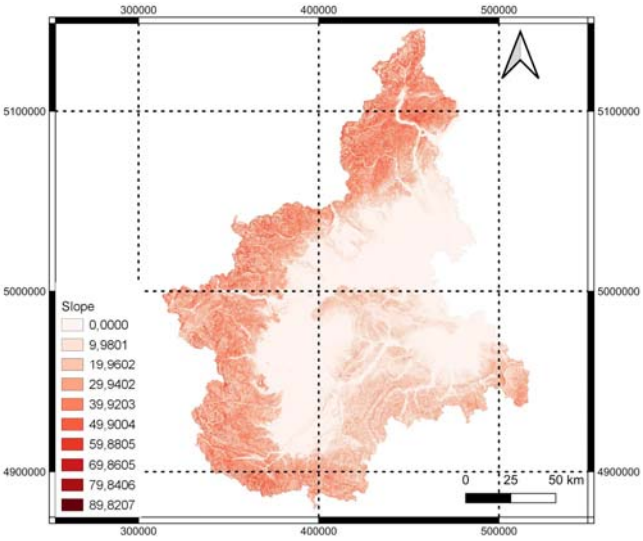

Fig. 7 Slope raster

- Calcareous schist: low grade metamorphic rock, formed by calcite, micas, biotite and quartz. The formation of the calcescisti with green stones or the Piemonte area is the set of rocks that originally constitute the seabed of the Ligurian-Piemontese Ocean. The deposits that by metamorphism gave rise to the calcescists were impure calcareous sediments (from clayey limestones to calcareous clays) deposited in the deep sea (lower Jurassic age)

In sedimentary rocks are included:

- Layers of marls: a terrigenous sedimentary rock composed of a clay and a limestone fraction, there are different types of marl depending on the percentages of limestone and clay. The terrigenous fraction derives from the washout of the continental areas adjacent to the sedimentation area or from the change of factory (from carbonate factory to pelagic factory), while the limestone fraction from calcium carbonate precipitation (middle Miocene age).

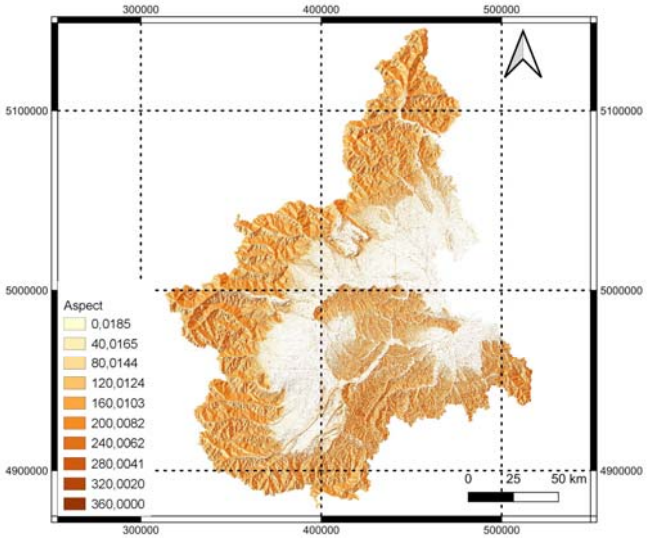

Fig. 8 Aspect raster

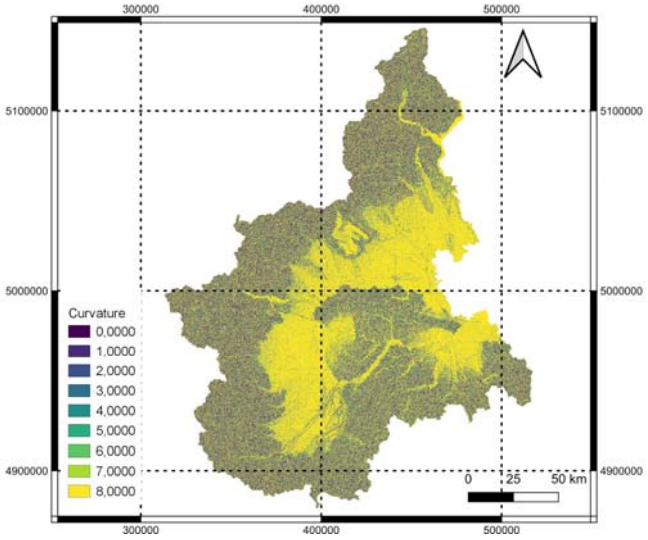

Fig. 9 Curvature raster

- Dolomite and limestone: sedimentary rocks with precipitation of $CaCO_3$ which is replaced by Mg at different percentages depending on the conditions of the water in which the sediment is found (upper Triassic age)

Land Cover/Land Use (LULC)

Another important fact is the use of the land. It is the land cover inventory and is divided into 44 classes (to improve visualization the classes are grouped into five categories in Fig. 11). They are described as vegetated, bare, wooded, cultivated areas, bodies of water, industrial areas, built up areas and road surfaces, and especially urban areas. The latter are

imported not only as they represent areas in which waterproofing is maximum with the increase in surface runoff and the collection of water. It is also important because it indicates the presence of people. This information was taken from the Corine Land Cover 2018 of the Copernicus system. See Fig. 11 for the corresponding raster of the study area of Piemonte.

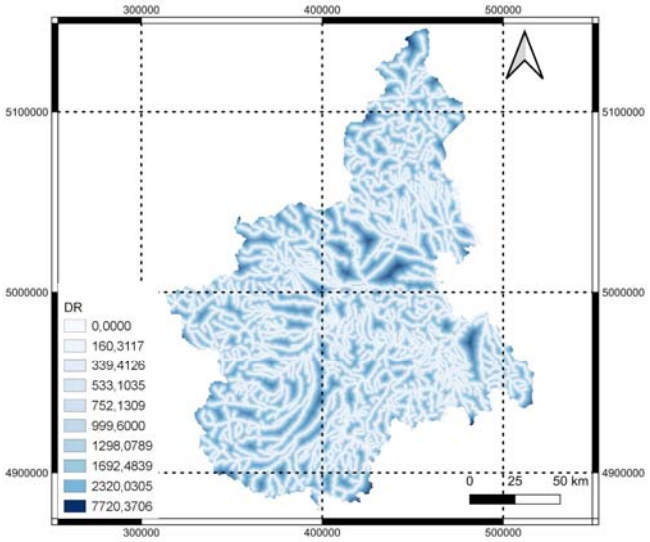

Fig. 10 Distance from River raster

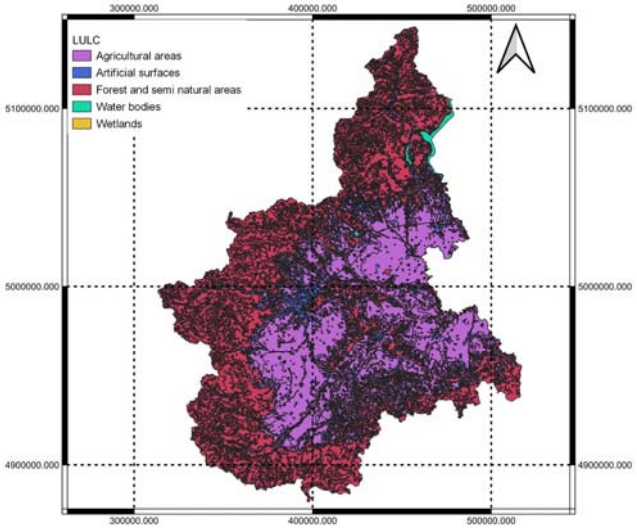

Fig. 11 Land Use/Land Cover raster

Frequency Ratio Mapping

For each static feature, we aimed to assess the relative importance of each range of values with respect to the flood chance. In order to achieve this, the frequency ratio approach was used, that is commonly used in landslide [18] and creates a mapping where each range of values in a feature can be substituted with its odds ratio of the event not occurring by chance.

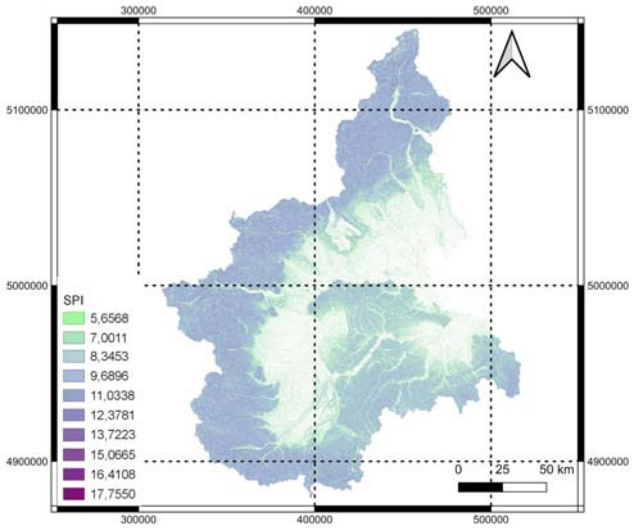

Fig. 12 SPI raster

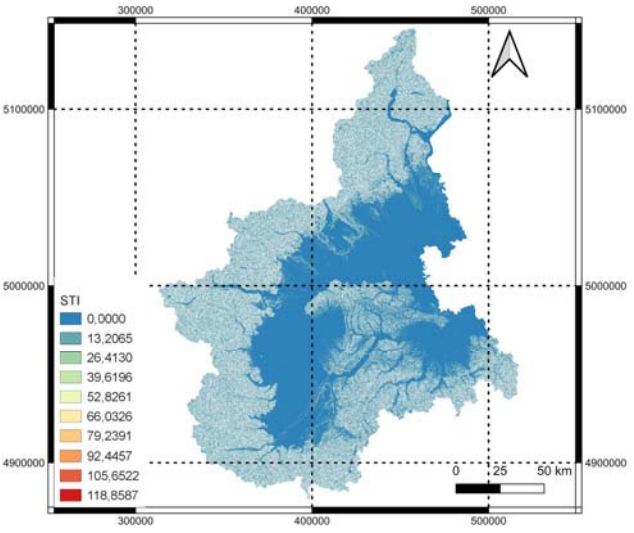

Fig. 13 STI raster

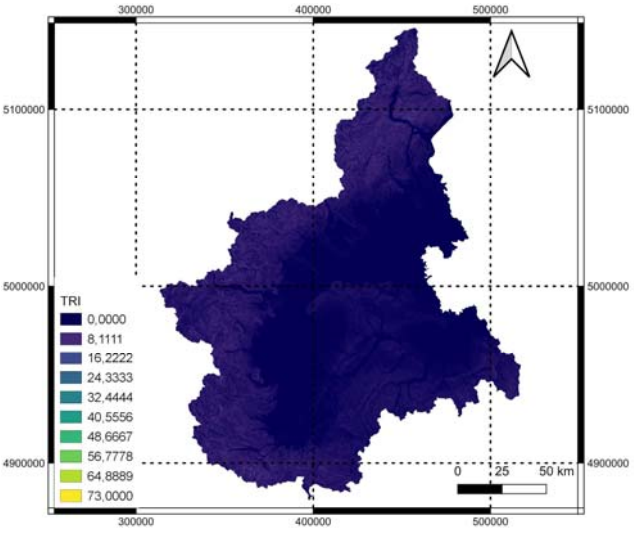

Fig. 14 TRI raster

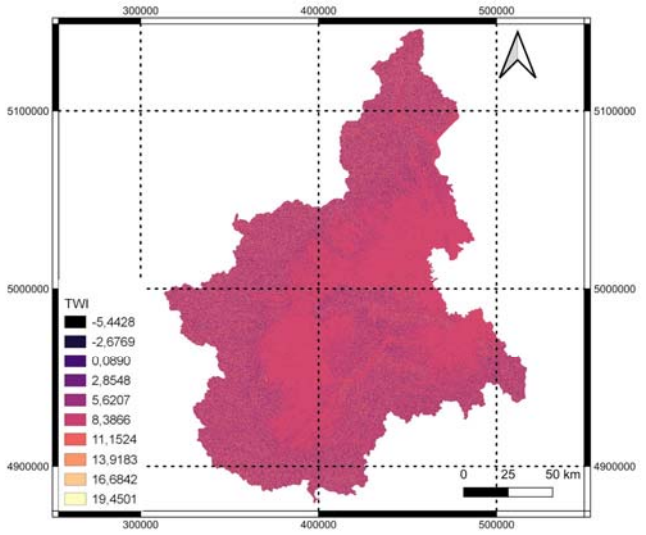

Fig. 15 TWI raster

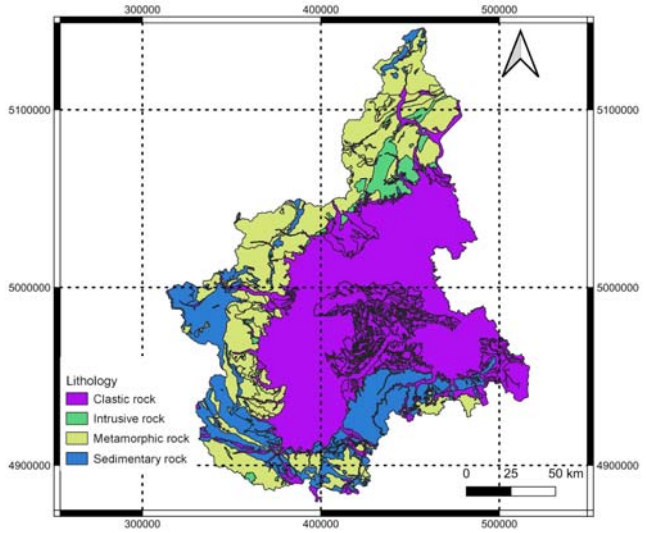

Fig. 16 Lithology raster

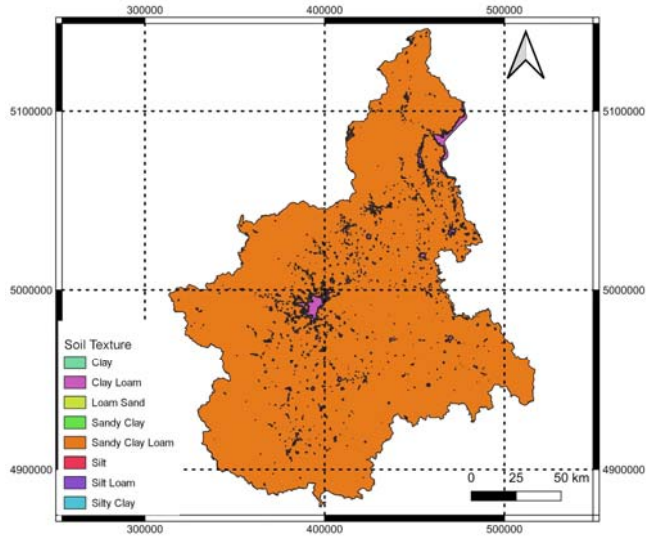

Fig. 17 Soil raster

Frequency ratio is defined as the ratio between two probabilities:

$$FR^i = \frac{P(event,i)}{P(event)\cdot P(i)} \simeq \frac{N^{event,i}/N^i}{N^{event}/N}$$

The first equality is obtained by using Bayes theorem and by considering our data as a pixel matrix with as many layers as the number of our features. This calculation can be done for each range of finite bins i, for each feature layer. Namely,

- $N^{event,i}$ is the number of pixels of class i that are also pixels containing a flood event
- N^i is the number of pixels of class i of the feature layer, that is the size of the i-th bin
- N^{event} is the number of pixels containing a flood event
- N is the total number of pixels considered (in the study area the whole Piemonte region)

Methods

In the study area of Piemonte the raster has a size of 26642 x 20367 pixels.

The raster has the following ratio:

- 288.969.353 outer pixels
- 253.648.261 inner pixels

As stated in the introduction the estimate of the flood hazard map of an area is achieved by getting the static data layers mapped to their FR counterparts as input features.

Train/Validation/Test split

The inner pixels have been randomly divided into three splits:

- training: 177.553.785 (70% of the dataset)
- validation: 50.729.654 (20% of the dataset)
- test: 25.364.822 (10% of the dataset)

The splitting is implemented to keep the ratio between the target values of the PAI layer (0, 1, 2 and 3) constant.

TABLE I
SPLIT OF THE PIEMONTE DATASET

Target value	Training	Validation	Test
0	166.283.309	47.509.517	23.754.757
1	8.163.717	2.332.491	1.166.244
2	1.293.817	369.662	184.831
3	1.812.942	517.984	258.990

In order to avoid any use of the test set in training the neural network, the train dataset is the only dataset used to compute frequency ratios.

Single Binary Output Models

Since the target hazard mapping has four different levels three different binary models have been implemented. The architecture is the same, whereas the outputs are the following

- model 1-2-3: detector of any flood event
- model 2-3: detector of medium and high frequency flood events
- model 3: detector of high frequency flood events

The model of a single hazard level detector is a multi-layer perceptron with a single hidden level with 16 neural units (see

Fig. 18 for the diagram of the architecture).

The activations of the hidden layer are rectified linear, whereas the output unit has a sigmoid activation, representing the probability of a flood event.

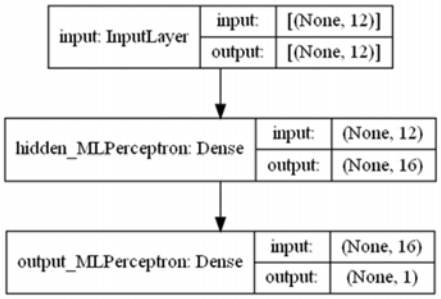

Fig. 18 Architecture of a single hazard level detector

The total number of trainable parameters is $225 = (12 + 1) \cdot 16 + (16 + 1) \cdot 1$ since biases are included as well.

Models' Combination

Since the target hazard mapping has four different levels, the three different binary models have been combined into one. The architecture is similar, whereas the outputs are the four probabilities of each flood hazard class (see Fig. 20 for the diagram of the architecture).

The last layer of this neural network has a softmax activation, σ, defined by:

$$\sigma(i) = \frac{e^{u_i}}{\sum_k e^{u_k}}$$

The special form of such activation normalizes the output (the sum over the units u_i is 1), therefore the response may be interpreted as probability distribution over predicted classes.

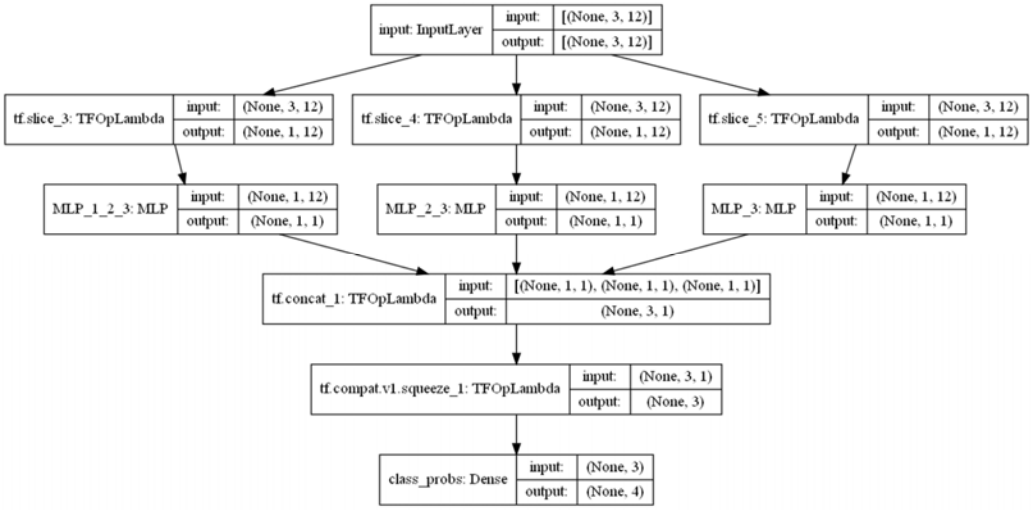

Fig. 19 Architecture multi flood hazard levels classifier

The total number of trainable parameters is $691 = 225 \cdot 3 + (3 + 1) \cdot 41$ since biases are included as well.

Performance Assessment

A baseline model, with no trainable parameters, whose decision is taken by the sum of the frequency ratios has been set as a benchmark for the performance of the model.

Since the flood hazard classes are strongly imbalanced, the loss function used for training has been endowed with weights $\{w_0, w_1\}$ defined by:

$$w_0 = \frac{\#pos + \#neg}{2 \cdot \#neg}$$
$$w_1 = \frac{\#pos + \#neg}{2 \cdot \#pos}$$

where $\#pos$ and $\#neg$ denote the positive and negative occurrences, respectively. Namely we have the following version of the binary cross-entropy:

$$CrossEntropy(pred, labels) = -\sum_{i\ in\ batch} w_{label_i} \cdot label_i \cdot log(pred_i)$$

We consider the following metrics:

- confusion matrix: collecting all the possible combinations of the classification, true positive TP, true negative TN, false positive FP, false negative FN
- F_1 score: a standard score used in statistical analysis of binary classification to measure the model's accuracy. It is defined as

$$F_1 = \frac{2}{\frac{1}{p}+\frac{1}{r}} = \frac{TP}{TP + \frac{1}{2} \cdot (FP + FN)}$$

where $p = \frac{TP}{TP+FP}$ and $r = \frac{TP}{TP+FN}$ denote the precision and recall, respectively.

- the model output for the two binary classes (flood vs. no flood)

The results of single event detectors are represented in Figs. 20-22.

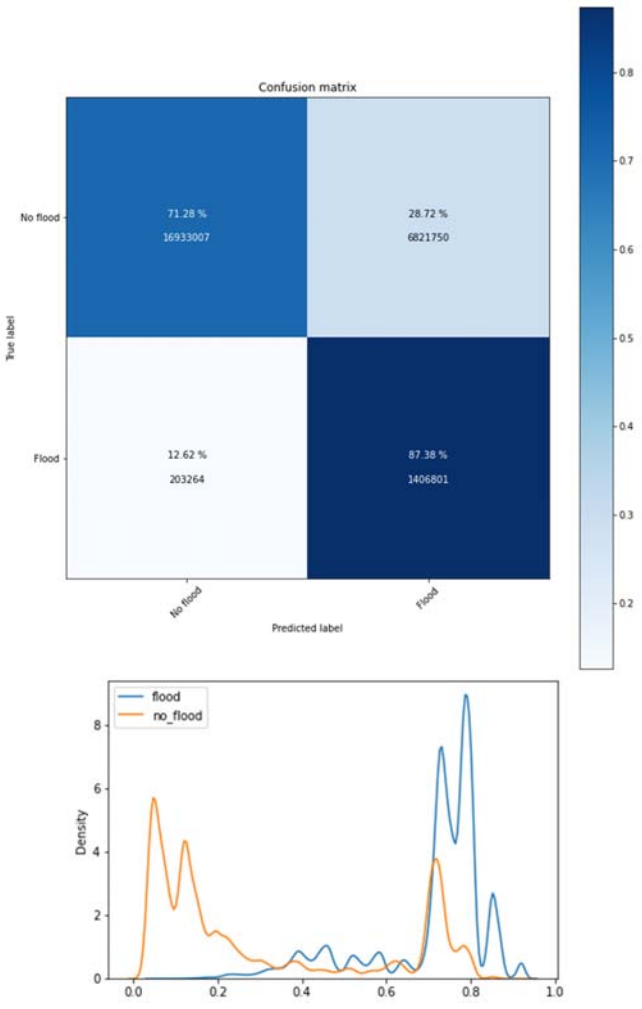

Fig. 20 Baseline detector of any flood event

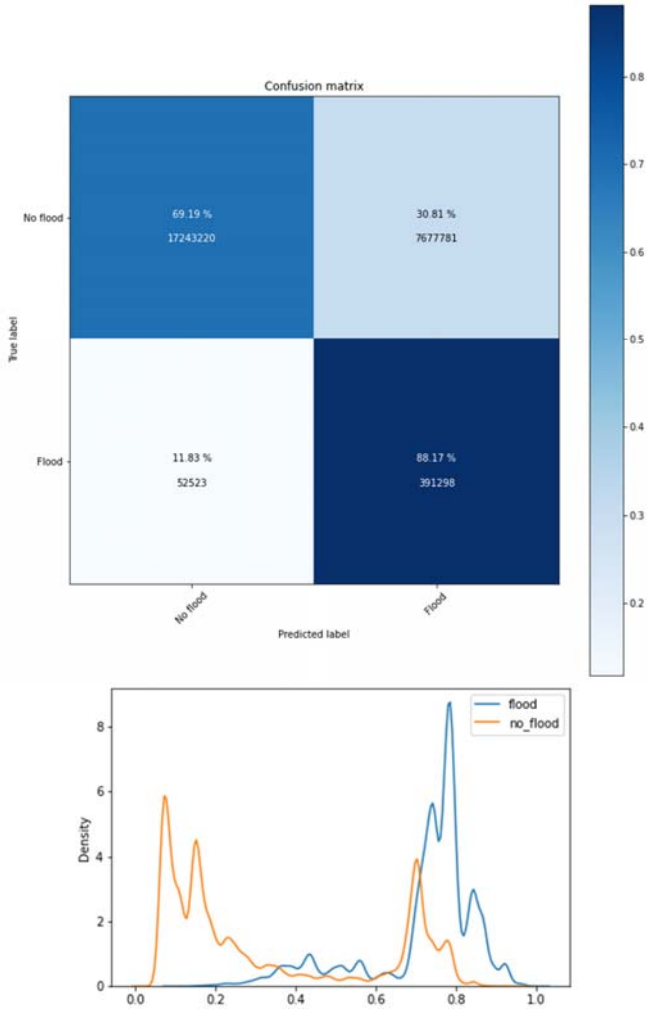

Fig. 21 Baseline detector of medium and high frequency flood events

TABLE II
BASELINE DETECTOR METRICS

	True negative	True positive	False negative	False positive	F_1
1-2-3	16933007 (71.28 %)	1406801 (87.38 %)	203264 (12.62 %)	6821750 (28.72 %)	0.286
2-3	17243220 (69.19 %)	391298 (88.17 %)	52523 (11.83 %)	7677781 (30.81 %)	0.092
3	16539679 (65.88 %)	244298 (94.33 %)	14692 (5.67 %)	8566153 (34.12 %)	0.054

Table II collects the indices of the three baseline models.

III. RESULTS

Frequency Ratio Mapping

Using the historical information by the train dataset the following mappings for the features are obtained. Tables III-XV collect the values of the frequency ratios obtained for the three binary models:

- 1-2-3: any flood events
- 2-3: medium and high frequency flood events
- 3: high frequency flood events

TABLE III
FREQUENCY RATIOS FOR ELEVATION

Bins	Frequency ratios		
	1-2-3	2-3	3
-10 m - 0 m	--	--	--
0 m - 50 m	--	--	--
50 m - 100 m	7.259	8.642	0.000
100 m - 200 m	2.751	3.010	3.061
200 m - 300 m	1.533	1.640	2.201
300 m - 500 m	0.663	0.223	0.381
500 m - 700 m	0.180	0.077	0.133
700 m - 1100 m	0.062	0.000	0.000
1100 m - 1500 m	0.003	0.000	0.000
1500 m - 2000 m	0.000	0.000	0.000
2000 m -5000 m	0.000	0.000	0.000

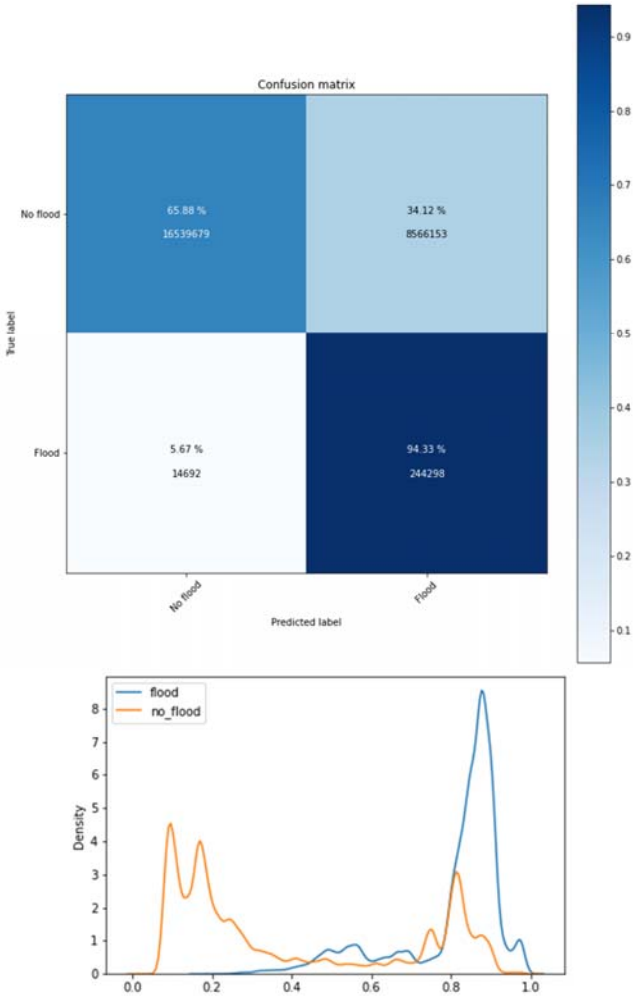

Fig. 22 Baseline detector of high frequency flood events

TABLE IV
FREQUENCY RATIOS FOR ASPECT

Bins	Frequency ratios		
	1-2-3	2-3	3
no direction	2.651	2.706	2.664
-22.5° - 22.5°	0.309	0.270	0.269
22.5° - 67.5°	0.287	0.253	0.274
67.5° - 112.5°	0.396	0.363	0.388
112.5° - 157.5°	0.301	0.282	0.322
157.5° - 202.5°	0.331	0.350	0.386
202.5° - 247.5°	0.207	0.192	0.209
247.5° - 292.5°	0.244	0.216	0.207
292.5° - 337.5°	0.214	0.173	0.180

TABLE V
FREQUENCY RATIOS FOR SLOPE

Bins	Frequency ratios		
	1-2-3	2-3	3
0° - 1.69°	2.653	2.708	2.666
1.69° - 4.49°	1.824	1.739	1.840
4.49° - 7.85°	0.307	0.199	0.240
7.85° - 11.9°	0.093	0.056	0.067
11.9° - 16.3°	0.039	0.026	0.035
16.3° - 21.1°	0.022	0.013	0.018
21.1° - 26.4°	0.015	0.009	0.013
26.4° - 33.1°	0.010	0.006	0.009
33.1° - 45.7°	0.005	0.002	0.003
> 45.7°	0.024	0.044	0.001

TABLE VI
FREQUENCY RATIOS FOR SPI

Bins	Frequency ratios		
	1-2-3	2-3	3
-1 - 0	2.653	2.708	2.666
0 - 2	--	--	--
2 - 4	--	--	--
4 - 6	1.921	1.876	1.959
6 - 8	0.753	0.696	0.747
8 - 10	0.044	0.029	0.032
10 - 12	0.011	0.005	0.007
12 - 14	0.005	0.001	0.002
14 - 16	0.003	0.000	0.000
16 - 18	0.002	0.000	0.000
18 - 20	0.000	0.000	0.000

TABLE VII
FREQUENCY RATIOS FOR TWI

Bins	Frequency ratios		
	1-2-3	2-3	3
< 0	0.027	0.030	0.004
0 - 0.96	0.037	0.028	0.031
0.96 - 5.47	0.331	0.303	0.328
5.47 - 6.08	0.041	0.028	0.033
6.08 - 6.62	0.049	0.031	0.042
6.62 - 7.07	0.052	0.029	0.038
7.07 - 7.53	0.049	0.025	0.034
7.53 - 7.99	0.053	0.021	0.030
7.99 - 8.45	0.041	0.018	0.025
8.45 - 9.057	0.032	0.012	0.017
9.057 - 9.89	2.192	2.227	2.203
> 9.89	0.188	0.168	0.179

TABLE VIII
FREQUENCY RATIOS FOR STI

Bins	Frequency ratios		
	1-2-3	2-3	3
< 0.0	0.022	0.015	0.017
0.0 - 0.5	2.503	2.555	2.516
0.5 - 1.0	1.133	1.105	1.154
1.0 - 1.5	0.867	0.843	0.869
1.5 - 2.0	0.149	0.114	0.125
2.0 - 3.0	0.575	0.515	0.562
3.0 -4.0	0.592	0.549	0.593
4.0 - 5.0	0.107	0.073	0.090
5.0 - 7.5	0.068	0.039	0.050
7.5 - 10.0	0.053	0.021	0.028
10.0 - 15.0	0.042	0.013	0.019
15.0 - 50.0	0.020	0.004	0.005
50.0 - 100.0	0.008	0.000	0.000
100.0 - 500.0	0.000	0.000	0.000

TABLE IX
FREQUENCY RATIOS FOR TRI

Bins	Frequency ratios		
	1-2-3	2-3	3
< 0	2.738	2.806	2.744
0.0 - 0.05	--	--	--
0.11 - 0.16	2.157	2.109	2.248
0.16 - 0.21	--	--	--
0.21 - 0.32	2.037	1.970	2.086
0.32 - 0.48	2.013	1.948	2.040
0.48 - 0.69	1.374	1.237	1.344
0.69 - 1.17	0.227	0.149	0.176
> 1.17	0.021	0.015	0.016

TABLE X
FREQUENCY RATIOS FOR CURVATURE

Bins	Frequency ratios		
	1-2-3	2-3	3
1	0.213	0.188	0.208
2	0.015	0.008	0.011
3	0.019	0.012	0.014
4	1.173	1.121	1.166
5	0.117	0.075	0.090
6	1.207	1.186	1.214
7	0.027	0.016	0.022
8	0.022	0.014	0.019
9	1.632	1.656	1.639

TABLE XI
FREQUENCY RATIOS FOR DISTANCE FROM RIVER

Bins	Frequency ratios		
	1-2-3	2-3	3
0 m - 281 m	2.849	3.210	2.797
281 m - 561 m	1.338	1.569	1.731
561 m - 842 m	0.711	0.638	0.826
842 m - 1122 m	0.434	0.288	0.390
1122 m - 1403 m	0.291	0.118	0.177
1403 m - 1683 m	0.257	0.058	0.097
1683 m - 1964 m	0.274	0.070	0.120
1964 m - 2244 m	0.276	0.036	0.062
2244 m - 2525 m	0.244	0.014	0.024
2525 m - 2806 m	0.223	0.000	0.000
2806 m - 3086 m	0.243	0.000	0.000
3086 m - 3367 m	0.250	0.000	0.000
3367 m - 3647 m	0.171	0.000	0.000
3647 m - 3928 m	0.102	0.000	0.000
3928 m - 4208 m	0.077	0.000	0.000
4208 m - 4489 m	0.071	0.000	0.000
4489 m - 4769 m	0.025	0.000	0.000
4769 m - 5050 m	0.105	0.000	0.000
5050 m - 5330 m	0.141	0.000	0.000
5330 m - 5611 m	0.001	0.000	0.000
5611 m - 5892 m	0.000	0.000	0.000
5892 m - 6172 m	0.000	0.000	0.000
6172 m - 6453 m	0.000	0.000	0.000
6453 m - 6733 m	0.000	0.000	0.000
6733 m - 7014 m	0.000	0.000	0.000
7014 m - 7294 m	0.000	0.000	0.000
7294 m - 7575 m	0.000	0.000	0.000
7575 m - 7855 m	0.000	0.000	0.000
> 7855 m	0.000	0.000	0.000

TABLE XII
FREQUENCY RATIOS FOR SOIL

Bins	Frequency ratios		
	1-2-3	2-3	3
Clay	15.069	0.000	0.000
Silty Clay	3.315	1.606	1.397
Silty Clay Loam	--	--	--
Sandy Clay	0.000	0.000	0.000
Sandy Clay Loam	0.986	0.986	1.001
Clay Loam	0.694	0.190	0.074
Silt	1.623	1.572	0.664
Silt Loam	1.618	1.922	1.437
Loam	--	--	--
Sand	--	--	--
Loamy Sand	3.502	0.000	0.000
Sandy Loam	--	--	--

The bins have been chosen without any assumption on the region, in order to let them be general enough, or at least to be applied all over the Italian territory. On the other hand, given the large size of the train dataset and the time span of the observations, it is likely to assume that the mapping will be constant.

TABLE XIII
FREQUENCY RATIOS FOR LITHOLOGY

Bins	Frequency ratios		
	1-2-3	2-3	3
Alluvial deposits in the plain and valley areas	2.023	4.770	0.000
Morainic deposits	2.581	2.578	2.593
Banks and clayey levels	0.008	0.002	0.004
Fine to medium sands	0.005	0.000	0.000
Clays and clayey marls	0.013	0.007	0.010
Layers of marl	0.029	0.036	0.026
Marly siltstones	0.015	0.000	0.000
Sandstones	0.013	0.021	0.013
Alternations of clays	0.004	0.000	0.000
Serpentinites	0.019	0.004	0.006
Calcescisti	0.000	0.000	0.000
Dolomite and limestone	0.000	0.000	0.000
Gneiss minutes	0.002	0.000	0.000
Gneiss occhiadini	0.004	0.000	0.000
Granites	0.001	0.000	0.000
Other	0.004	0.002	0.004

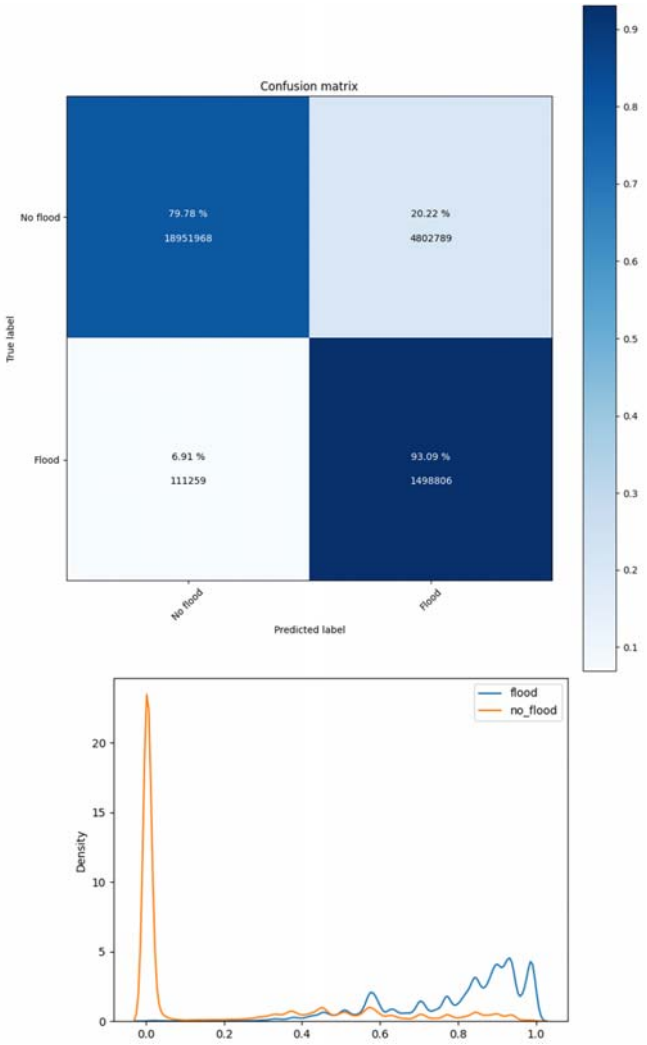

Fig. 23 Neural network detector of any flood event

TABLE XIV
FREQUENCY RATIOS FOR LAND USE/LAND COVER

Bins	Frequency ratios		
	1-2-3	2-3	3
Continuous urban fabric	1.066	0.157	0.265
Discontinuous urban fabric	1.004	0.361	0.559
Industrial or commercial units	1.765	1.350	2.057
Road and rail networks and associated land	2.441	1.972	3.062
Port areas	--	--	--
Airports	0.000	0.000	0.000
Mineral extraction sites	4.531	9.515	10.585
Dump sites	0.453	0.000	0.000
Construction sites	0.000	0.000	0.000
Green urban areas	3.020	0.946	0.000
Sport and leisure facilities	2.520	3.835	5.886
Non-irrigated arable land	2.173	2.348	2.858
Permanently irrigated land	--	--	--
Rice fields	2.520	0.598	0.849
Vineyards	0.094	0.005	0.008
Fruit trees and berry plantations	2.222	0.020	0.034
Olive groves	--	--	--
Pastures	1.450	0.232	0.397
Annual crops associated with permanent crops	0.370	0.000	0.000
Complex cultivation patterns	0.796	0.559	0.847
Land principally occupied by agriculture, with significant areas of natural vegetation	1.378	1.582	1.716
Agro-forestry areas	--	--	--
Broad-leaved forest	0.340	0.422	0.322
Coniferous forest	0.006	0.000	0.000
Mixed forest	0.024	0.024	0.000
Natural grasslands	0.014	0.004	0.000
Moors and heathland	0.000	0.000	0.000
Sclerophyllous vegetation	--	--	--
Transitional woodland-shrub	0.859	1.424	0.616
Beaches, dunes, sands	13.786	21.337	11.531
Bare rocks	0.000	0.000	0.000
Sparsely vegetated areas	0.000	0.001	0.000
Burnt areas	0.000	0.000	0.000
Glaciers and perpetual snow	0.000	0.000	0.000
Inland marshes	8.268	18.343	0.000
Peat bogs	--	--	--
Salt marshes	--	--	--
Salines	--	--	--
Intertidal flats	--	--	--
Water courses	13.050	32.225	14.881
Water bodies	0.139	0.380	0.517
Coastal lagoons	--	--	--
Estuaries	--	--	--
Sea and ocean	--	--	--
Nodata	1.715	3.410	0.000

Flood Hazard Map

The results of single event detectors are represented in Figs. 23-25.

The percentages of both the true negatives and the true positive are improved, and the F_1 score is doubled with respect to the corresponding baseline models (see Table II). Absolute low values of F_1 are connected with a large size of false positive cases. That is not so critical as would be the opposite case of a higher number of false negatives, since overestimation of the flood hazard may bring to a safer map. On the other hand, underestimating flood hazard leads to a very unsafe map.

As stated before, the binary detectors can be combined to build a multi-level classification model. The binary detectors are used to initialize the combined model. The confusion matrix coming out at the end of the training is shown in Fig. 26.

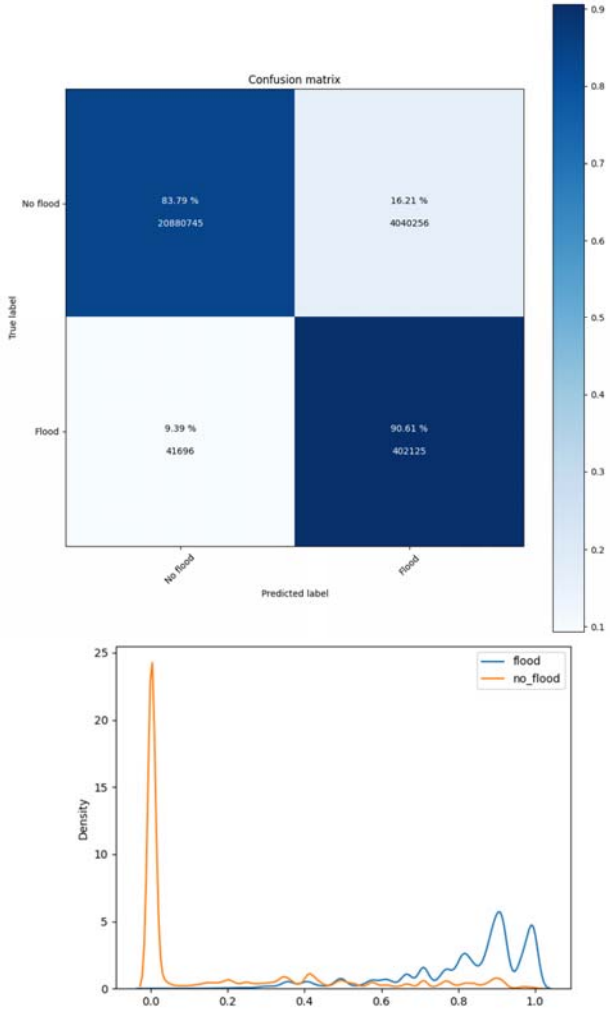

Fig. 24 Neural network detector of medium and high frequency flood events

Table XV collects the indices of the three neural network models.

Principal Component Analysis

The errors of the combined model were further analyzed. The first two principal components were considered of the test dataset, since the variance explained is large enough (see Fig. 27).

We focused on the no flood events of the test dataset, without loss of generality. The scatter plot of the two components has been used to depict how features are linearly separable according to the predicted flood hazard risk (Figs. 27-34). In order to improve the visualization figures have been coupled, Figs. 28, 30, 32, 34 represent the points where the model fails, whereas in Figs. 29, 31, 33, 35 every point is represented.

The predicted classes are represented by the following colors:

- Flood hazard level 0: orange
- Flood hazard level 1: green
- Flood hazard level 2. red
- Flood hazard level 3: blue

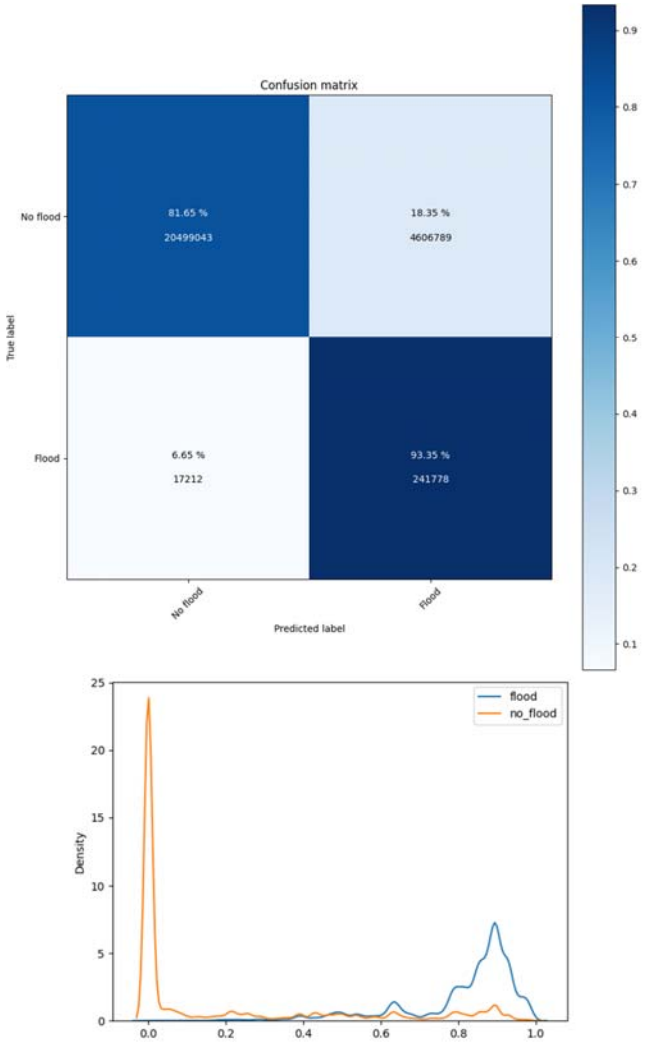

Fig. 25 Neural network detector of high frequency flood events

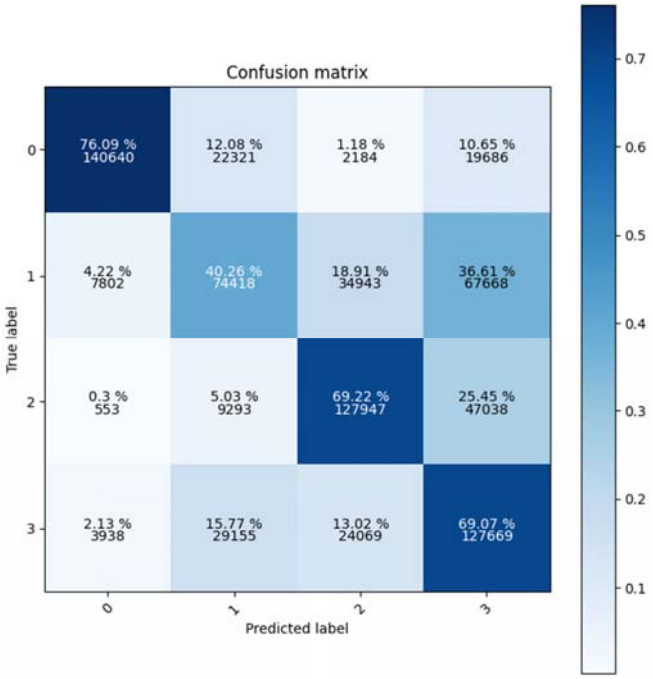

Fig. 26 Confusion matrix for the multi-level classification model

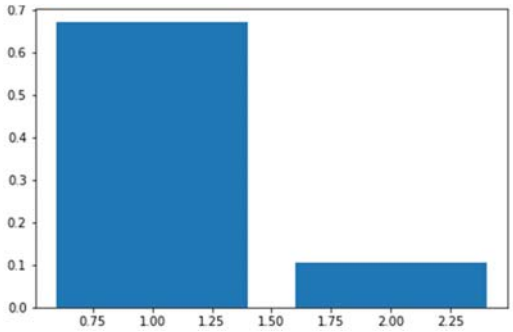

Fig. 27 Explained variance for the first 2 principal components (test dataset)

TABLE XV
NEURAL NETWORK MODELS METRICS

	True negative	True positive	False negative	False positive	F_1c
1-2-3	18951968 (79.78 %)	1498806 (93.09 %)	111259 (6.91 %)	4802789 (20.22 %)	0.379
2-3	20880745 (83.79 %)	402125 (90.61 %)	41696 (9.39 %)	4040256 (16.21 %)	0.165
3	20499043 (81.65 %)	241778 (93.35 %)	17212 (6.65 %)	4606789 (18.35 %)	0.095

It turns out that level 0 lies on the lower left corner, and level 2 on the upper right corner. Level 1 and level 3 both lie on the center, and the overlapping is an explanation for the model confusion between these two levels.

IV. CONCLUSION

This work proposed a different modelling strategy for flood hazard maps, combining classical (FR, Frequency Ratio) and modern (Neural Networks) approaches. The binary models all perform well, surely helped by the feature space remodulation induced by the FR transformation, but their combination trained to produce a multi-class classification suffered from an inherent degree of indistinguishability given by the data, as shown by the PCA analysis. These results indicate that an efficient flood hazard modeling should be enriched by more information coming from independent sources (remember that most of our data were derived from the DTM) like vegetation indices (NDVI, dNBR) or anthropic data.

The classification power of the benchmark model based only on FRs has been improved by the mixture with a neural network. That is a first step in enabling automation of flood hazard mapping.

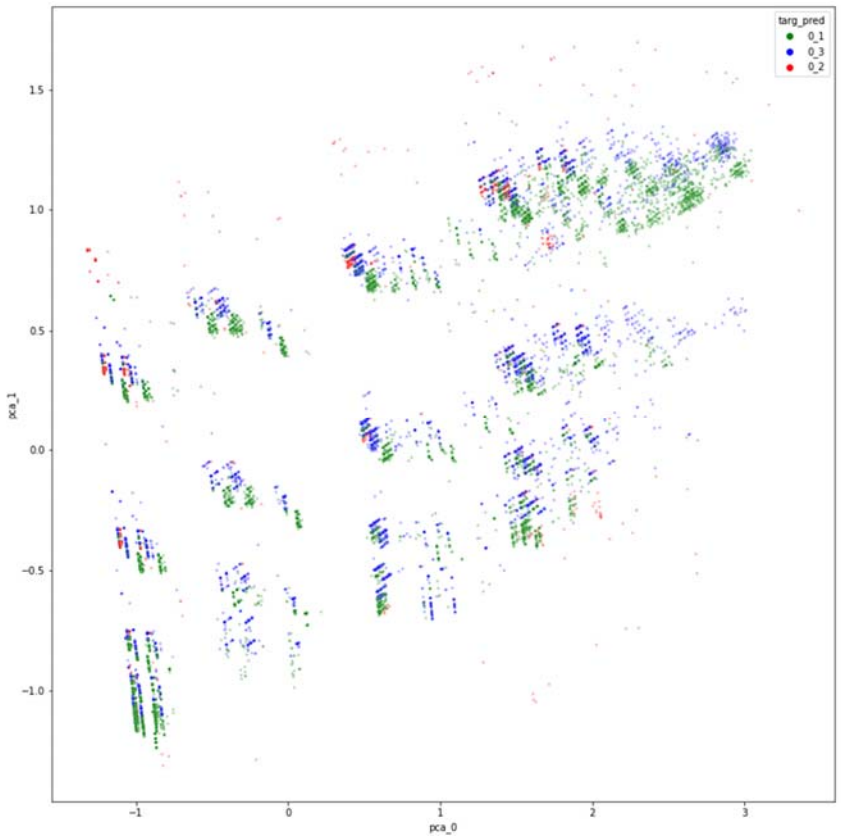

Fig. 28 Scatter plot of the first 2 principal components for level 0, without true positives

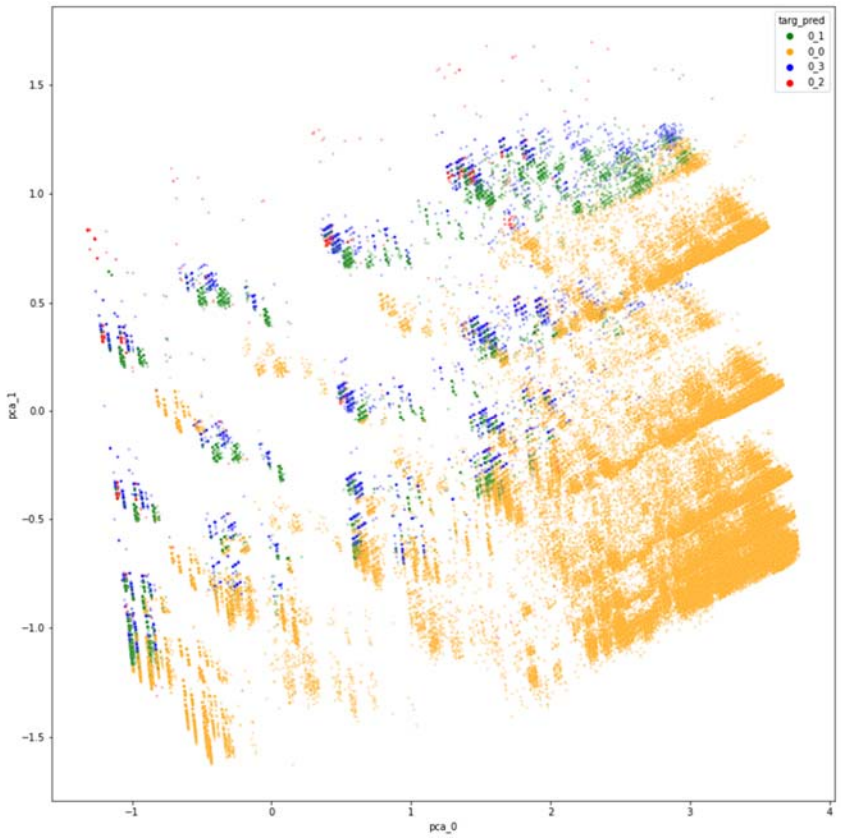

Fig. 29 Scatter plot of the first 2 principal components for level 0, with true positives (orange)

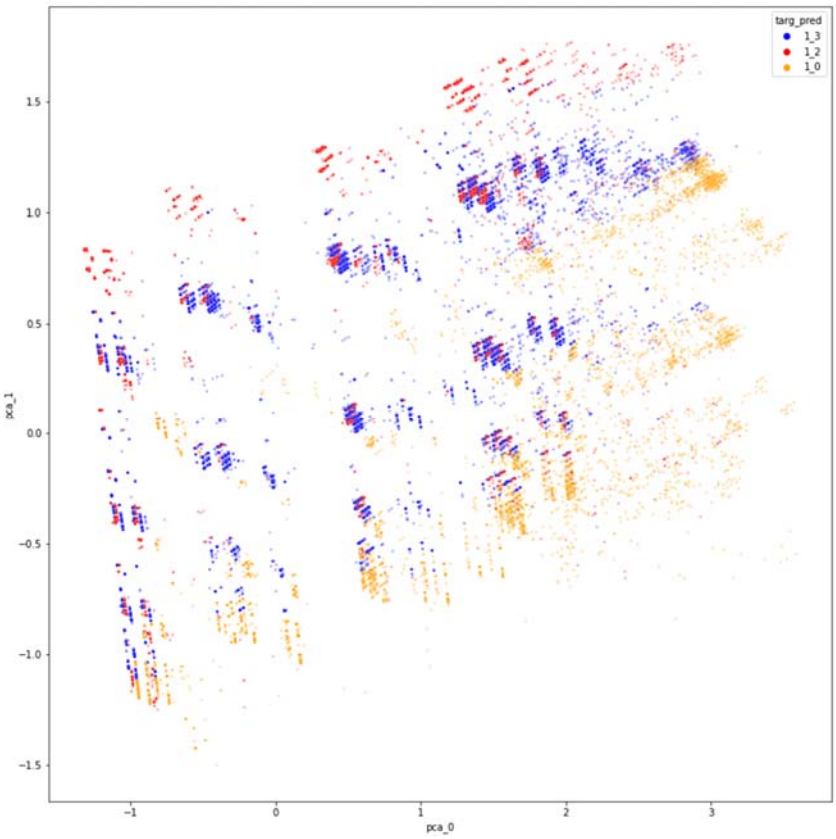

Fig. 30 Scatter plot of the first 2 principal components for level 1, without true positives

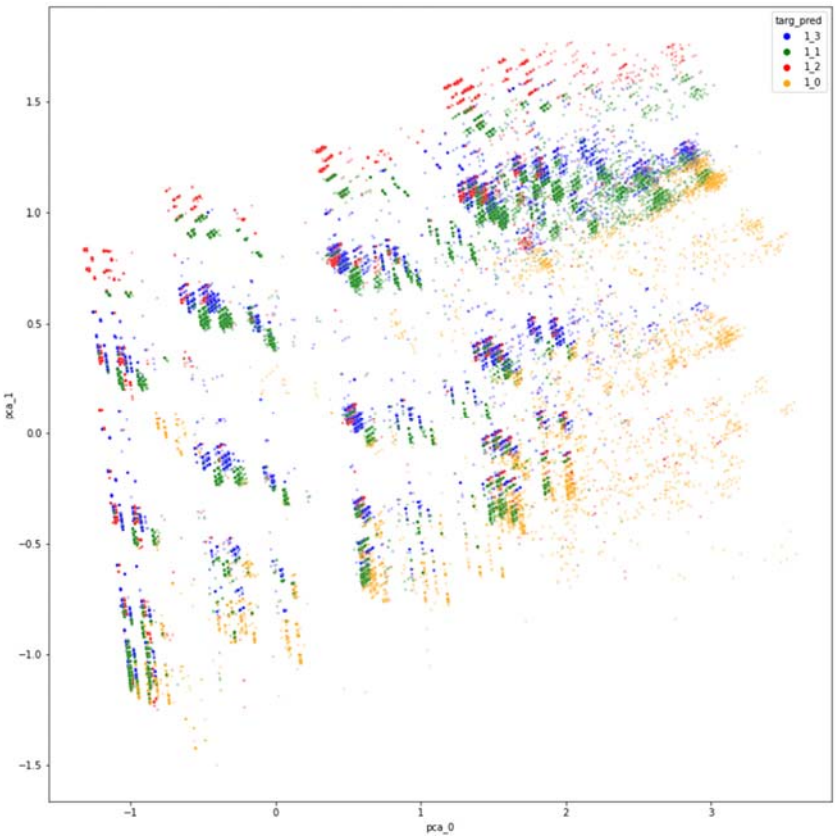

Fig. 31 Scatter plot of the first 2 principal components for level 1, with true positives (green)

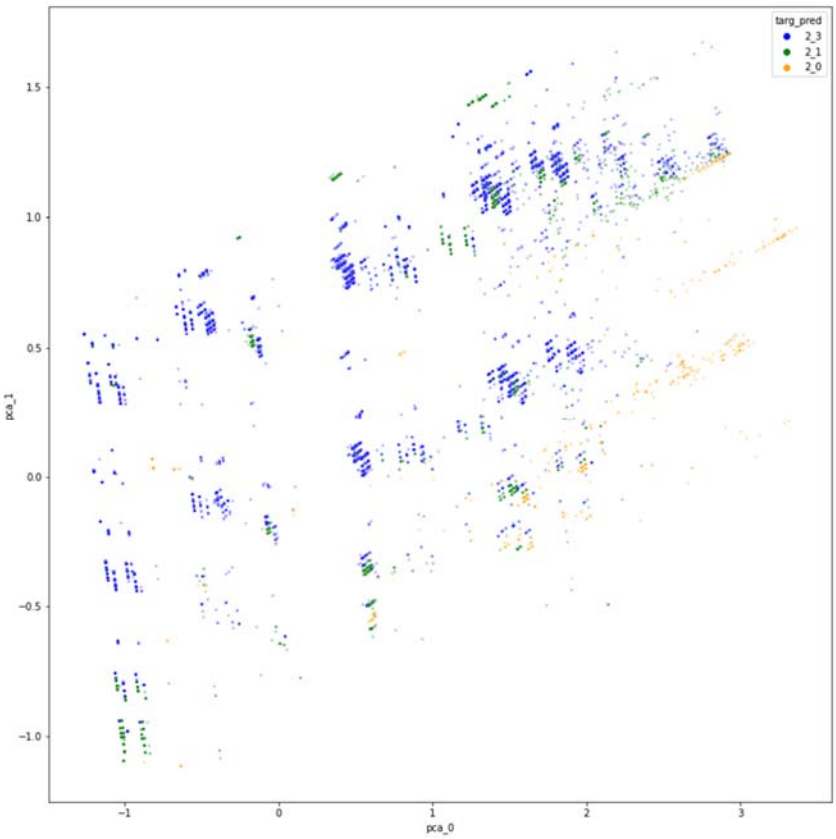

Fig. 32 Scatter plot of the first 2 principal components for level 1, without true positives

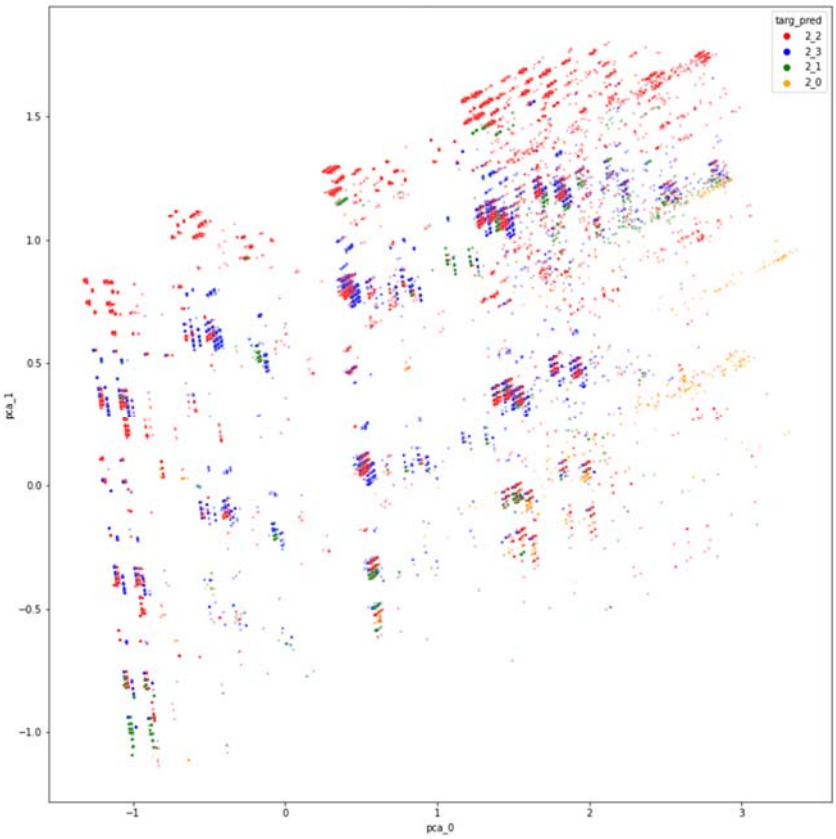

Fig. 33 Scatter plot of the first 2 principal components for level 1, with true positives (red)

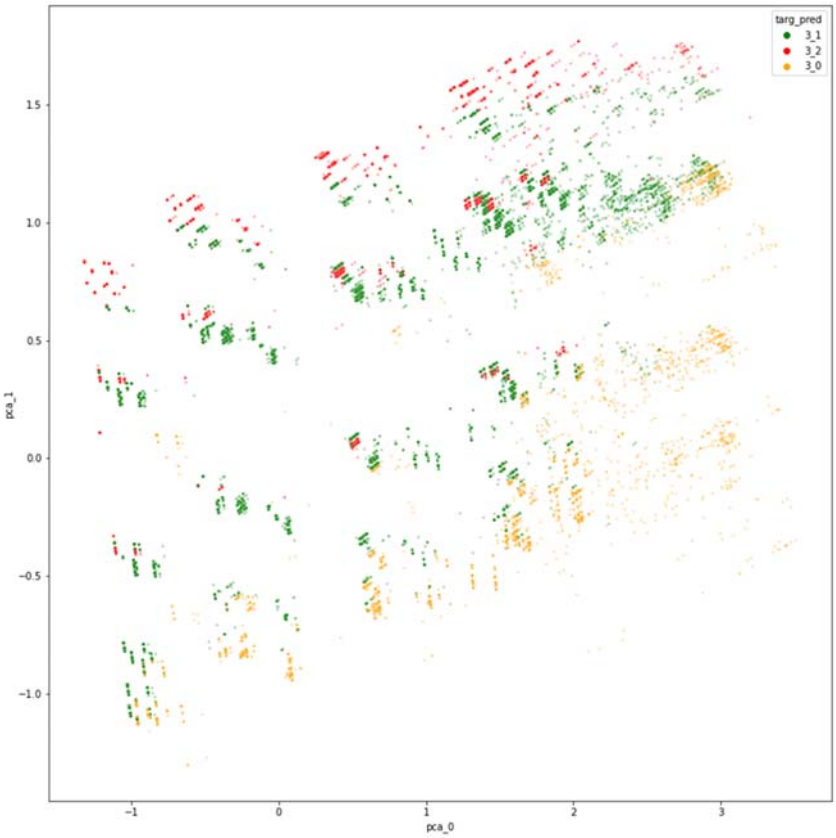

Fig. 34 Scatter plot of the first 2 principal components for level 3, without true positives

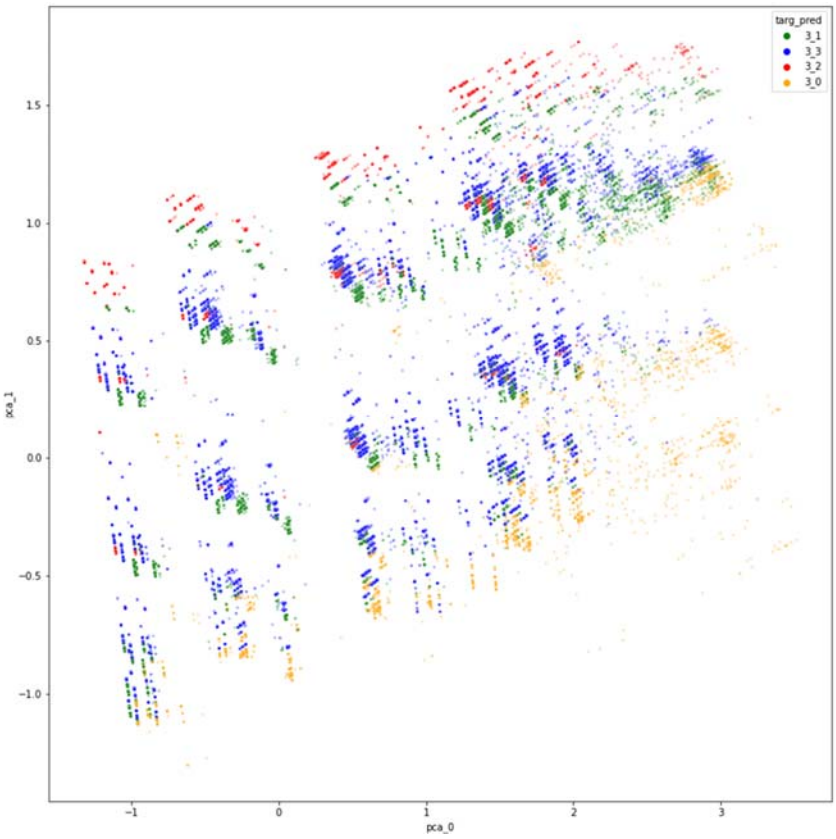

Fig. 35 Scatter plot of the first 2 principal components for level 3, with true positives (blue)

VI. Future Work

There are many research directions to be explored in the field of flood modeling.

The first problem to tackle is to overcome linear separation. A wider feature space (with less correlation between data) could surely benefit the whole model. A larger input including the neighborhoods of the central pixel could be mixed with convolutional layers to improve the classification capacity.

As far as classification of multiple flood hazard levels is concerned, a different architecture could be investigated without the combination of single binary detectors.

References

[1] D. Judi, C. Rakowski, S. Waichler, Y. Feng and M. Wigmosta, «Integrated Modeling Approach for the Development of Climate-Informed, Actionable Information,» Water, vol. 10, n. 6, p. 775, 13 June 2018.

[2] S. A. Schumm and R. W. Lichty, «Time, space, and causality in geomorphology,» American Journal of Science, vol. 263, n. 2, pp. 110-119, February 1965.

[3] K. Li, S. Wu, E. Dai and Z. Xu, «Flood loss analysis and quantitative risk assessment in China,» Natural Hazards, vol. 63, n. 2, pp. 737-760, September 2012.

[4] G. Testa, D. Zuccalà, F. Alcrudo, J. Mulet and S. Soares-Frazão, «Flash flood flow experiment in a simplified urban district,» Journal of Hydraulic Research, vol. 45, pp. 37-44, 2007.

[5] E. van Beek and J. van Alphen, «From flood defence to flood management - prerequisites for sustainable flood management,» in Floods, from defence to management: Proceedings of the 3rd International Symposium on Flood Defence, Leiden, 2006.

[6] W.-H. Teng, M.-H. Hsu, C.-H. Wu and A. S. Chen, «Impact of Flood Disasters on Taiwan in the Last Quarter Century,» Natural Hazards, vol. 37, n. 1-2, pp. 191-207, 2006.

[7] C. Kousky, «Financing Flood Losses: A Discussion of the National Flood Insurance Program,» vol. 21, n. 1, pp. 11-32, 2018.

[8] D. R. Dassanayake, A. Burzel and H. Oumeraci, «Methods for the Evaluation of Intangible Flood Losses and Their Integration in Flood Risk Analysis,» Coastal Engineering Journal, vol. 57, n. 1, pp. 1-35, 2015.

[9] V. Meyer, S. Scheuer e and D. Haase, «A multicriteria approach for flood risk mapping exemplified at the Mulde river, Germany,» Natural Hazards, vol. 48, n. 1, pp. 17-39, 2009.

[10] M.-J. Lee, J.-e. Kang and S. Jeon, «Application of frequency ratio model and validation for predictive flooded area susceptibility mapping using GIS,» in 2012 IEEE International Geoscience and Remote Sensing Symposium, July, 2012.

[11] A. K. Kar, A. Lohani, N. Goel and G. Roy, «Rain gauge network design for flood forecasting using multi-criteria decision analysis and clustering techniques in lower Mahanadi river basin, India,» Journal of Hydrology: Regional Studies, vol. 4, pp. 313-332, September 2015.

[12] M. Ahmadlou, A. Al-Fugara, A. R. Al-Shabeeb, A. Arora, R. Al-Adamat, Q. B. Pham, N. Al-Ansari, N. T. T. Linh and H. Sajedi, «Flood susceptibility mapping and assessment using a novel deep learning model combining multilayer perceptron and autoencoder neural networks,» Journal of Flood Risk Management, vol. 14, n. 1, March 2021.

[13] H. Mojaddadi Rizeei, B. Pradhan, H. Nampak, N. Ahmad and A. Halim bin Ghazali, «Ensemble machine-learning-based geospatial approach for flood risk assessment using multi-sensor remote-sensing data and GIS,» Geomatics, Natural Hazards and Risk, 1 3 2017.

[14] M. E. Ritter, The physical environment: An introduction to physical geography, 2003.

[15] A. Piloyan and M. Konečný, «Semi-Automated Classification of Landform Elements in Armenia Based on SRTM DEM using K-Means Unsupervised Classification,» Quaestiones Geographicae, vol. 36, n. 1, pp. 93-103, March 2017.

[16] I. D. Moore and G. J. Burch, «Physical Basis of the Length-slope Factor in the Universal Soil Loss Equation,» vol. 50, n. 5, pp. 1294-1298, 1986.

[17] S. J. Riley, S. D. Degloria e R. Elliot, «A Terrain Ruggedness Index that Quantifies Topographic Heterogeneity,» Intermountain Journal of Science, vol. 5, pp. 23-27, 1999.

[18] A. R. Rasyid, N. P. Bhandary and R. Yatabe, «Performance of frequency ratio and logistic regression model in creating GIS based landslides susceptibility map at Lompobattang Mountain, Indonesia,» Geoenvironmental Disasters, vol. 3, n. 1, p. 19, December 2016.

[19] Soil Science Division Staff, «Soil survey manual,» United States Department of Agriculture, Washington, D.C., 1993.

[20] «Soil Grids,» (Online). Available: https://soilgrids.org/.